Available online at www.sciencedirect.com

ScienceDirect

journal homepage: www.elsevier.com/locate/he

Aerosol-assisted chemical vapor deposition of nickel sulfide nanowires for electrochemical water oxidation

Muhammad Ali Ehsan [a,*], *Abuzar Khan* [a], *Muhammad Nadeem Zafar* [b,**], *Usman Ali Akber* [a], *Abbas Saeed Hakeem* [a], *Muhammad Faizan Nazar* [c]

[a] *Interdisciplinary Research Center-Hydrogen and Energy Storage (IRC-HES), King Fahd University of Petroleum and Minerals, Dhahran, 31261, Saudi Arabia*

[b] *Department of Chemistry, University of Gujrat, Gujrat, 50700, Pakistan*

[c] *Department of Chemistry, University of Education Lahore, Multan Campus, 60700, Pakistan*

HIGHLIGHTS

- Time dependent fabrication of NiS via aerosol assisted chemical vapor deposition.
- NiS-90 min variant exhibited remarkable oxygen evolution reaction (OER) activity.
- Partial transformation NiS into more active NiO was responsible for efficient OER.

GRAPHICAL ABSTRACT

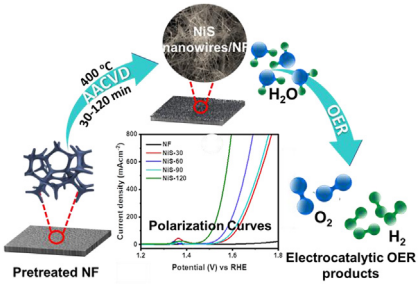

ARTICLE INFO

Article history:
Received 27 July 2021
Received in revised form
24 September 2021
Accepted 28 October 2021
Available online 19 November 2021

Keywords:
Aerosol assisted
Chemical vapor deposition
Electrocatalyst
Nanowires
Water oxidation
Overpotential

ABSTRACT

Slow kinetics and emotive design of electrocatalysts are the main barriers to effective oxygen evolution and hydrogen production from water. To overcome these challenges, nickel sulfide impregnated electrocatalysts with auxiliary structural features have recently attracted attention as effective alternatives for the oxygen evolution reaction (OER). Herein, nickel sulfide (NiS) nanowires are developed directly on nickel foam (NF), which have proven to be a highly efficient electrocatalyst for OER in an alkaline medium. For this, NiS nanowires were grown on NF for short intervals of 30, 60, 90 and 120 min through an aerosol-assisted chemical vapor deposition (AACVD) process using nickel diethyldithiocarbamate as a precursor. The as-developed NiS electrode showed excellent OER activity in 1.0 M KOH solution. It is noteworthy that the NiS electrode produced after 90 min provides a reference current density of 10 mA cm^{-2} at an overpotential (η) of 210 mV and achieves a higher current density of 500 mA cm^{-2} at an overpotential of 340 mV. Moreover, the nanocatalyst has observed a low Tafel value (60 mV dec^{-1}) and good OER stability. After the electrolysis, it was found that the surface of the NiS catalyst was partially modified into

* *Corresponding author.*
** *Corresponding author.*
E-mail addresses: meali@kfupm.edu.sa (M.A. Ehsan), nadeem.zafar@uog.edu.pk, znadeempk@gmail.com (M.N. Zafar).
https://doi.org/10.1016/j.ijhydene.2021.10.231

nickel oxide. The S atom in the NiS catalyst can provide an activator function that first converts the sulfide to a hydroxide and then eventually becomes an oxyhydroxide species. The more active nickel hydroxide/oxyhydroxide phase raises the water oxidation performance to a new level. The facile synthesis of NiS nanowire films by AACVD tends to be used as an anodic material in various other power generation and energy conversion devices such as batteries, fuel cells, and supercapacitors.

Introduction

The scarcity of fossil fuels and their impact on environmental pollution have pushed the world to explore green and sustainable energy routes. Due to its high energy density, hydrogen is considered as the most convincing substitute for traditional fossil fuels [1,2]. In particular, the use of hydrogen as a fuel guarantees zero emission of CO_2 and minimizes greenhouse gases in order to make the earth hygienic, healthy, and green [3]. Hydrogen can be converted into ammonia, whose use as a fuel is being investigated [4]. Currently, hydrogen is largely extracted from hydrocarbon-based fossil fuels such as coal, oil, and natural gas, which emit a large portion of the CO_2 directly into the air. Thus, the hydrogen produced in this way increases the amount of toxic gases in the air and cannot meet the requirement for ecological sustainability [5]. Alternatively, the hydrogen generated from water electrolysis is a renewable method that doesn't contain the environment and has great potential to meet global energy needs over longer periods of time [6].

In general, water dissociation occurs in two half-cell redox steps called the hydrogen evolution reaction (HER) and oxygen evolution reaction (OER). Large-scale water splitting remains a challenge due to the slow kinetics of the OER, which must be intensified with the help of a highly stable and active catalyst in order to generate high oxygen concentrations through low overpotentials [7,8]. Precious metals oxides such as RuO_2 and IrO_2 are naturally blessed to catalyze OER at low overpotentials and are therefore regarded as benchmark electrocatalysts in this domain [2,9,10]. However, their high cost, low bulk, and poor stability are certain disadvantages that limit their use on a commercial scale. Therefore, the development of inexpensive, stable, and high-performance OER catalysts for remarkable water splitting are sought.

To address these issues, various earth-rich OER electrocatalysts based on transition metals [11,12] such as metal oxides/hydroxides [13–16], perovskites [17–19], chalcogenides [20–22], carbides [23,24], phosphates [25–27] and molecular electrocatalysts [28–30] have been studied intensively. It has been observed that nickel-based nanomaterials actively participate in energy storage and conversion applications [31–33]. In this regard, the nickel chalcogenides have gained considerable importance because of their wonderful electronic structures and their propensity for multiphase. In addition, the low price, radial availability, and accessibility of nickel compounds have increased their popularity for energy-based applications [34–37].

In particular, nickel sulfide in various forms, including Ni_3S_2, NiS, and NiS_2 has shown potential for OER catalysis [38–40]. It is worth noting that the synthesis of nickel sulfide on conductive supports such as Ni foam (NF), graphene or carbon cloth etc. has dramatically improved the OER activity [41–44]. The porous 3D cross-linked architecture of NF provides a large accessible active site, minimizes catalyst agglomeration, and improves electron transfer rates, resulting in improved electrocatalytic OER performance [45,46]. Recently, Ni_3S_2 nanorods developed on NF have shown excellent OER activity [47]. The higher catalytic activity was due to the formation of several mixed oxidation states of Ni including Ni°, Ni^{+}, and Ni^{2+} as well as to the synergetic chemical bond that developed between the different phases of the Ni_3S_2 nanorod/NiO layer and the NF support. On the other hand, it was also found that the manufacturing process and the concentration of sulfur in the nickel sulfide compound have a positive influence on the OER activity [48]. For instance, the Ni_xS_y film made by pulse electrodeposition was evaluated for OER catalysis. It was observed that the nickel sulfide catalyst was completely converted into a highly active amorphous nickel oxide phase in the electrochemical oxidation process and that sulfide ions were depleted from the catalyst surface [49]. Although several important studies have been performed to uncover the catalytic activity of the Ni_3S_2 catalyst, its performance is still limited by its inherent problems such as particles aggregation, limited active sites, and low conductivity [50]. Therefore, it is important to find efficient ways to address these challenges and ultimately develop nickel sulfide catalyst with improved OER performance.

Inspired by previous studies, here we evaluate the OER performance of NiS nanowires obtained directly on a NF surface by means of one-step aerosol-assisted chemical vapor deposition (AACVD). Although several reports on the synthesis of specialized precursors and their use in AACVD to produce nickel sulfide thin films are known [51–53], these films have not been investigated for electrochemical water oxidation purposes. AACVD is a viable approach to produce catalytic thin films of controlled thickness and to distinguish morphologies in the shortest possible time. Like the other manufacturing processes such as electrodeposition, calcination, and hydrothermal, AACVD enables porous NF to be used as the substrate surface. However, the catalyst synthesis via AACVD is quick and easy compared to the conventional hydrothermal process [54–56]. Instead of sulfurizing the NF with elemental S or thiourea, as observed in hydrothermal technology, AACVD consumes the nickel diethyldithiocarbamate compound ($Ni(S_2CN(C_2H_5)_2)$) as a single source precursor (SSP). Both the Ni and S atoms in SSP decompose simultaneously on the NF surface to produce a NiS product that is completely different from the common nickel sulfide (Ni_3S_2) obtained

through hydrothermal processes and the catalyst loading can be carefully monitored as the deposition time increases. It is noteworthy that the obtained NiS nanowire catalyst after 90 min of AACVD process showed remarkable OER performance with lowest overpotential of 210 mV to reach the standard current density of 10 mA cm^{-2} and a higher current density of 500 mA cm^{-2} was reached at an overpotential of 340 mV. In addition, the catalyst performed the OER continuously for 19 h, which shows its excellent stability under electrochemical conditions.

Experimental

Materials and chemicals

Nickel (II) nitrate hexahydrate [$Ni(NO_3)_2{\cdot}6H_2O$] and sodium diethyldithiocarbamate hydrate $NaS_2CN(C_2H_5)_2).xH_2O$ from Sigma Aldrich were used as received. Methanol and toluene from Merck chemicals were used during the synthesis of the nickel diethyldithiocarbamate precursor and for the fabrication of nickel sulfide thin films in the AACVD process.

Synthesis of nickel diethyldithiocarbamate precursor

In a typical experiment, 500 mg (2.22 mmol) sodium diethyldithiocarbamate ($NaS_2CN(C_2H_5)_2$)) was dissolved in 30 mL methanol, followed by the addition of 321 mg (1.10 mmol) $Ni(NO_3)_2{\cdot}6H_2O$. The green solution thus obtained was stirred at room temperature for 30 min. The reaction mixture was filtered, and the filtrate was slowly evaporated until the green crystals of the desired precursor $Ni(S_2CN(C_2H_5))_2$ were obtained in two days. The precursor without prior characterization was used directly in AACVD to produce NiS catalyst.

Preparation of NiS catalyst thin films by AACVD

The methanol solution of the precursor $Ni(S_2CN(C_2H_5))_2$ served as the feedstock for aerosol-assisted chemical vapor deposition (AACVD). The catalyst synthesis was carried out on a nickel foam (NF) substrate of size (1×2 cm^2) at a temperature of 400 °C. The mass loading of the catalyst was controlled by changing the deposition time periodically every 30, 60, 90 and 120 min. For this, the weight of the NF substrate was measured with a microanalytical balance before and after the deposition experiment.

The experimental setup and operation of AACVD was described in our earlier work [56,57]. Briefly, the precursor feed was placed in a two-neck round bottom flask immersed in a water bath of an ultrasonic humidifier equipped with a piezoelectric modulator. The aerosol vapor generated in this setup was injected into the reaction chamber. The aerosol flowed over a preheated NF substrate in the reaction chamber (400 °C) and formed the desired NiS deposits. During the entire deposition process, nitrogen gas (99.99% purity) was used at a flow rate of 110 mL/min. Apparently the black mass was deposited evenly on the NF. The deposition time was varied between 30 and 120 min and the samples obtained were labeled as NiS-30, NiS-60, NiS-90 and NiS-120. After completion of the deposition process, the mass of the catalyst produced was immediately recorded and determined as follows: 0.08 mg cm^{-2} (NiS-30), 0.18 mg cm^{-2} (NiS-60), 0.3 mg cm^{-2} (NiS-90) and 0.45 mg cm^{-2} (NiS-120). The catalyst mass is observed to increase with deposition time, indicating the higher growth rates of CVD reactions over longer periods of time.

Characterization of NiS catalysts

The crystal structure of the NiS catalyst was determined by Rigaku CuKα radiation using a benchtop MiniFlex X-ray diffraction (mini-XRD) instrument. The thin film morphologies were examined on a dual beam field emission scanning electron microscope TESCAN Lyra 3. Elemental detection was performed using Energy Dispersion X-ray (EDX) spectroscopy on EDX, INCA Energy 200, Oxford Instrument. The surface chemistry and oxidation state of the NiS catalyst were examined by X-ray photoelectron spectroscopy (XPS). For this, the Thermos Scientific Escalab 250Xi spectrometer equipped with a monochromatic Al Kα (1486.6 eV) X-ray source with a resolution of 0.5 eV was used.

Electrochemical OER studies

The electrochemical measurements of the NiS electrocatalyst were recorded using Gamry INTERFACE 1010 E Potentiostat. The typical three-electrode cell was constituted; the NiS electrode developed on NF served as a working electrode together with a platinum coil and Ag/AgCl as a counter and reference electrode, respectively. All electrochemical experiments such as cyclic voltammetry (CV), linear sweep voltammetry (LSCV) and chronopotentiometry (CP) were performed in 1.0 M KOH solution. For the durability test, chronopotentiometry measurements were carried out at two different current values over several hours. The electrochemical impedance spectroscopy (EIS) was performed in the frequency range of 100 kHz to 0.1 Hz at open circuit potential using amplitude value of 10 mV.

Results and discussion

Characterization of NiS catalysts

Fig. 1 shows the XRD patterns of as-prepared nickel sulfide samples, NiS-30, NiS-60, NiS-90 and NiS-120. In XRD patterns, the characteristic reflections (100), (101), (102), (110) and (202) located at $2\theta = 30.5°$, 35.0°, 46.0°, 53.5° and 73.4° correspond to the monocrystalline NiS in hexagonal phase (ICSD no. 002-1280). No other impurity peaks such as metallic Ni and NiO were detected in XRD patterns, indicating the successful conversion of nickel diethyldithiocarbamate to pure NiS products without the need for an additional sulfurization process. Initially, the NiS-30 sample showed two broad XRD peaks at $2\theta = 30.5°$ and 46.0°, which became strong and intense as the deposition time increased, and some additional and important peaks appeared in the 120-min developed sample. The observation suggests that the crystallinity of the sample improves with increasing deposition time.

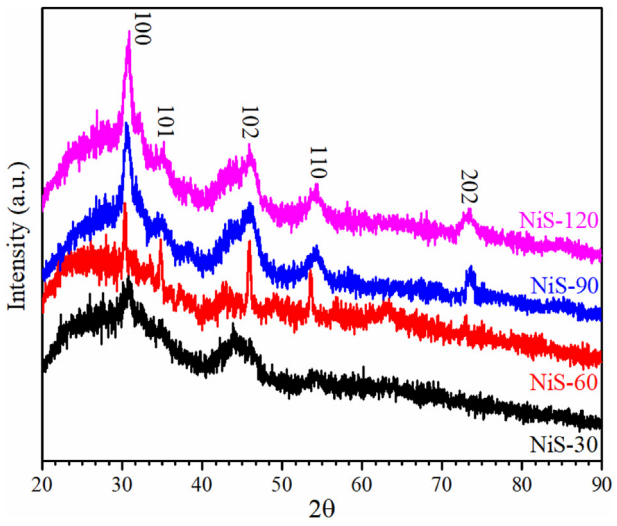

Fig. 1 – XRD patterns of nickel sulfide samples, NiS-30, NiS-60, NiS-90 and NiS-120 deposited via AACVD for periods of 30, 60, 90 and 120 min, respectively.

The NiS microstructure produced on the NF surface by varying deposition time was examined with FESEM and the corresponding micrographs are shown in Fig. 2. Low-magnification FESEM images, Fig. 2 ((a)–(d)), clearly reflect the change in growth behavior of the NiS deposits over time. The morphologies are well connected to the NF surface. In the first 30 min, the NF struts receive copious amounts of NiS nanocrystallites and globe-shaped objects grow on the uneven spots of NF. This structure tends to grow from the same center to produce thick nanocrystallites and large spherical objects when the time extends to 60 min. After 90 min, the NF pores are densely covered with nanocrystallite flakes of NiS, which form a fur-rug shaped structure, as shown in Fig. 2c. Finally, at 120 min, the NF top skeleton is completely covered with spherical, berry-like features protruding from the NF surface. The corresponding high-resolution FSEM images of NiS samples (Fig. 2 (a1)–(d1)) show a view of entangled, conglutinated and disordered nanowires, and this nanostructure remains in all NiS samples.

In AACVD, thin film microstructures are generally transformed with increasing calcination/deposition time due to the application of the additional thermal energy. In the present case, however, the nanowire structure remains sable if the calcination periods are increased from 30 to 90 min, and no significant change is observed in high-resolution FESEM images, Fig. 2 (a1–c1). However, the NiS sample prepared after 120 min shows some growth of nanoribbons like features in the upper surface, but the nanowire prints below are also visible (Fig. 2 (d1)). Interestingly, the nanowires are stacked to form a three-dimensional (3D) structure, which, compared to other nanostructures, has a better conductivity and a higher surface-to-volume ratio [58]. The catalyst comprising such morphological features exhibits improved catalytic activity and prolongs durability in OER catalysis.

The elemental composition of the NiS sample was verified by energy dispersive X-ray analysis (EDX). Fig. 3 shows the EDX spectra of all NiS samples with the measured concentrations of Ni and S elements. In the NiS-30 sample, the Ni concentration is very high compared to S, which is due to the nickel contribution of the NF surface. As the thickness of the NiS deposit increases over time, the contribution of nickel from the NF substrate surface decreases. It is worth noting that no oxygen is detected in these samples and NiS is the only product made in all cases.

XPS analysis was performed on a NiS-90 sample to better understand the chemistry of the surface components. The high-resolution spectra of Ni 2p and S 2p are shown in Fig. 4.

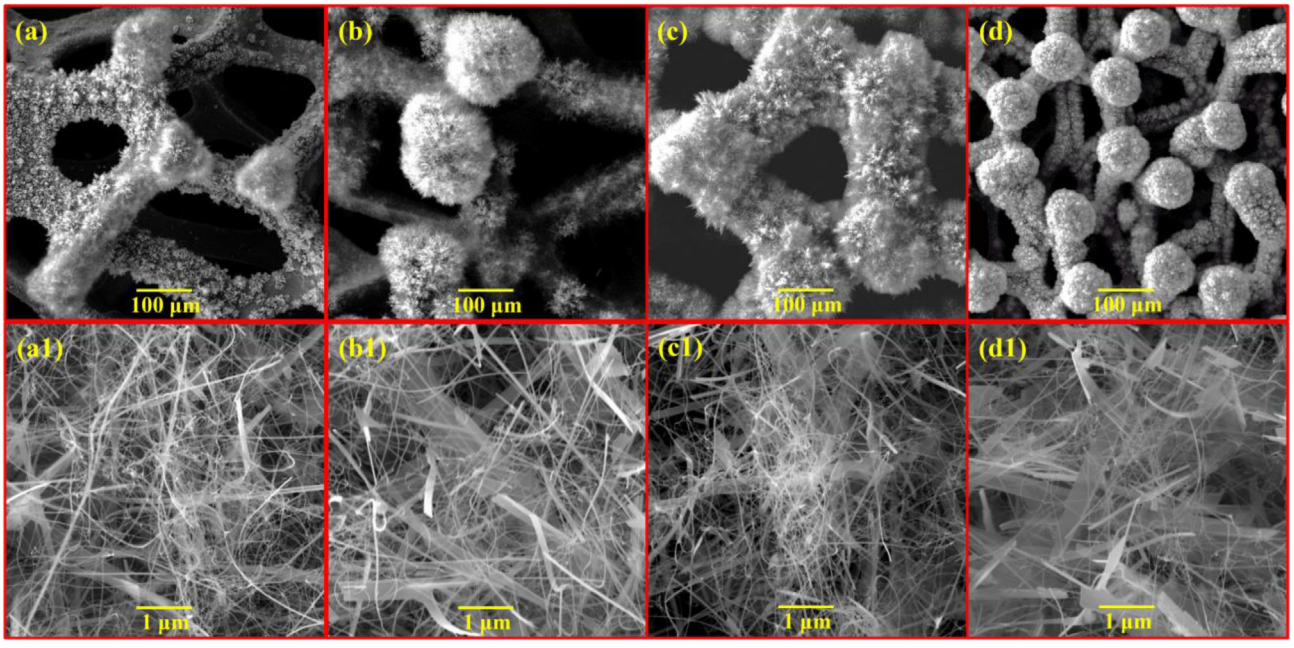

Fig. 2 – FESEM images of NiS deposits on a nickel foam substrate for various deposition times of; (a, a1) 30 min, (b, b1) 60 min, (c, c1) 90 min and (d, d1) 120 min. (a–d) low-magnification (1.0 Kx); (a1-d1) high-magnification (50 Kx).

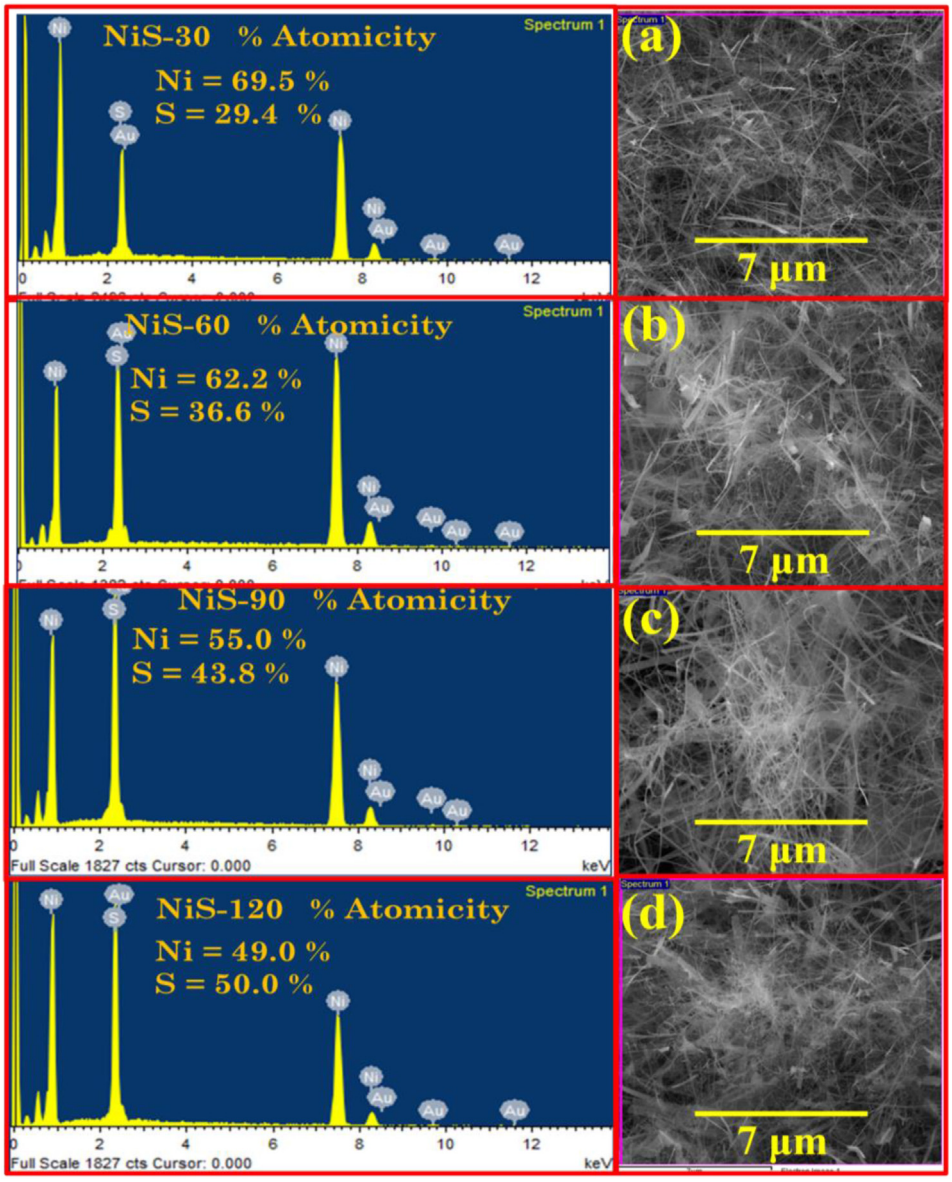

Fig. 3 – EDX spectra of different NiS samples prepared on nickel foam substrate (a) NiS-30, (b) NiS-60, (c) NiS-90 and (d) NiS-120.

The Ni 2p spectrum shown in Fig. 4 (a) shows two spin-orbit doublet peaks for Ni $2p_{3/2}$ and Ni $2p_{1/2}$ at 855.4 and 873.4 eV, respectively. The corresponding satellite peaks are observed at 861.3 and 879.5 eV, which suggests the presence of Ni^{2+} species [47]. A small shoulder peak at 853.1 eV besides Ni $2p_{3/2}$, corresponds to the characteristic peak for NiS [59,60]. The S2p spectrum in Fig. 4 (b) shows a binding energy value of 162.3 eV. The fitting peak at around 162.3 eV belongs to S $2p_{3/2}$, and the peak at 163.5 eV is assigned to S $2p_{1/2}$ [61]. These values agree with previous reports of NiS [62]. The XPS result confirms the observations from those of the XRD pattern and confirms the presence of a pure NiS deposit.

Electrochemical water oxidation of NiS nanowires electrodes

The catalytic performance of electrodes made from as-synthesized NiS nanowires was examined by the electrochemical water oxidation performance in an alkaline 1.0 M KOH solution. Initially, all NiS catalyst electrodes were electrochemically activated by performing cyclic voltammetry (CV) in the potential range of 1.0–1.8 V (RHE). Each NiS electrode was scanned for fifty consecutive CV cycles and the results of the 1st and 50th profiles are overlaid in Fig. 5. All catalyst samples showed anodic peaks between 1.3 and 1.5 V_{RHE} due to the oxidation of Ni species into Ni(II)/Ni (III) (*i.e.* $Ni(OH)_2$ to NiOOH) [45,63–65]. It is worth noting that the amplitude of this peak increases with each CV cycle. This suggests that the electrochemical oxidation of NiS creates more catalytically active spices in the form of NiOOH on the NF surface. The increase in the catalytic sites leads to an improvement in the overpotential and the current density of the catalyst. A final current density ~1000 mA cm^{-2} at a potential 1.7 V (Vs RHE) was achieved with each NiS electrode. Remarkably, the NiS-90 electrode exhibited superior activity

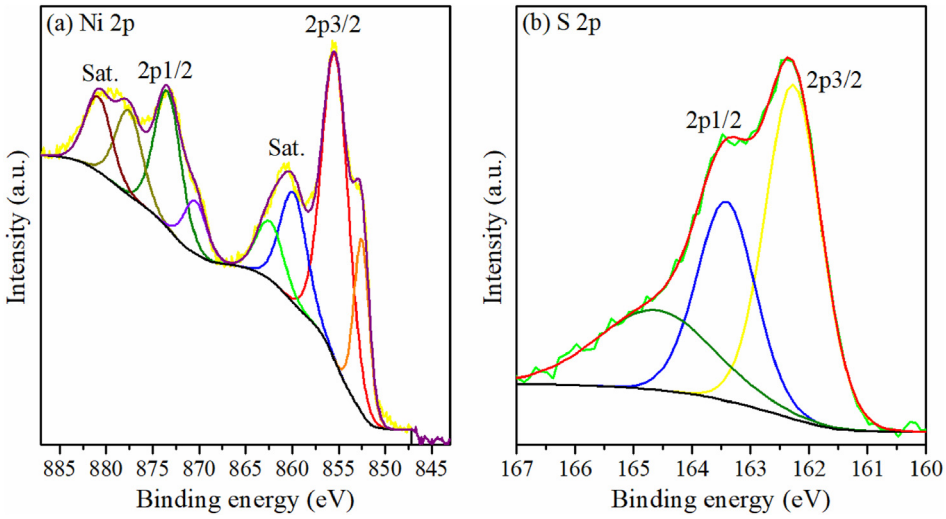

Fig. 4 – High-resolution XPS spectra of NiS-90 sample; (a) Ni 2p spectrum, (b) S 2p spectrum.

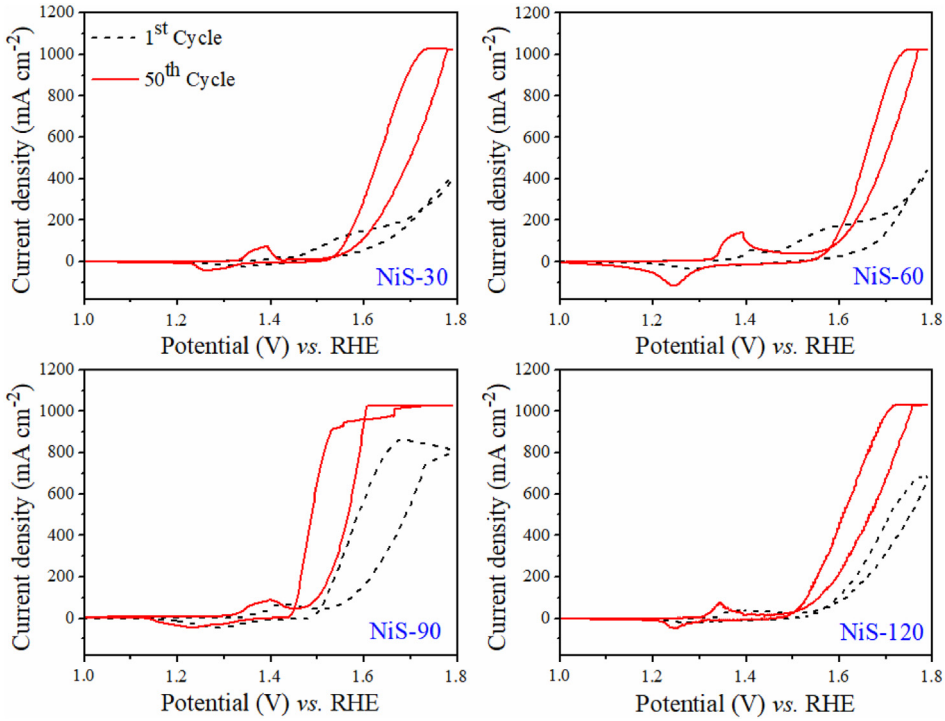

Fig. 5 – Cyclic voltammetry (CV) scans for various NiS catalysts; NiS-30, NiS-60, NiS-90 and NiS-120 electrodes, 1st CV cycle (dash black line) and 50th CV cycle (solid red line). The CV was performed at a scan rate of 50 mV s^{-1}. (For interpretation of the references to colour in this figure legend, the reader is referred to the Web version of this article.)

and the current density of 1000 mA cm^{-2} was reached even before 1.6 V (Vs RHE) and no further current density could be measured because the maximum current sensing capacity of the potentiostat was 1 A.

Fig. 6 (a) shows the polarization curves (Linear Sweep Voltammetry) of the electrochemically activated NiS electrodes, which were carried out with a scan rate of 10 mV s^{-1}. To confirm the OER catalytic activity, the overpotential (η) of all catalysts at current densities of 10 and 500 mA cm^{-2} were compared (Fig. 6 (b)). It can be seen from the polarization curves that NiS-90 catalyst clearly outperformed other NiS catalyst by exhibiting the lowest overpotential (η_{10}) of 210 mV. The observed trend for OER activity was as follows: Bare NF (η_{10} 495 mV) ‹ NiS-30 (η_{10} 290 mV) = NiS-120 (η_{10} 290 mV) ‹ NiS-60 (η_{10} 270 mV) and NiS-90 (η_{10} 210 mV). A similar trend was observed when overpotential (η_{500}) values were evaluated and the NiS-90 catalyst displayed a smallest η_{500} of 340 mV. It is worth noting that the OER kinetics of NiS-30 and NiS-120 electrodes is almost the same, and their overpotential (η_{10} and η_{50}) and current densities are almost comparable.

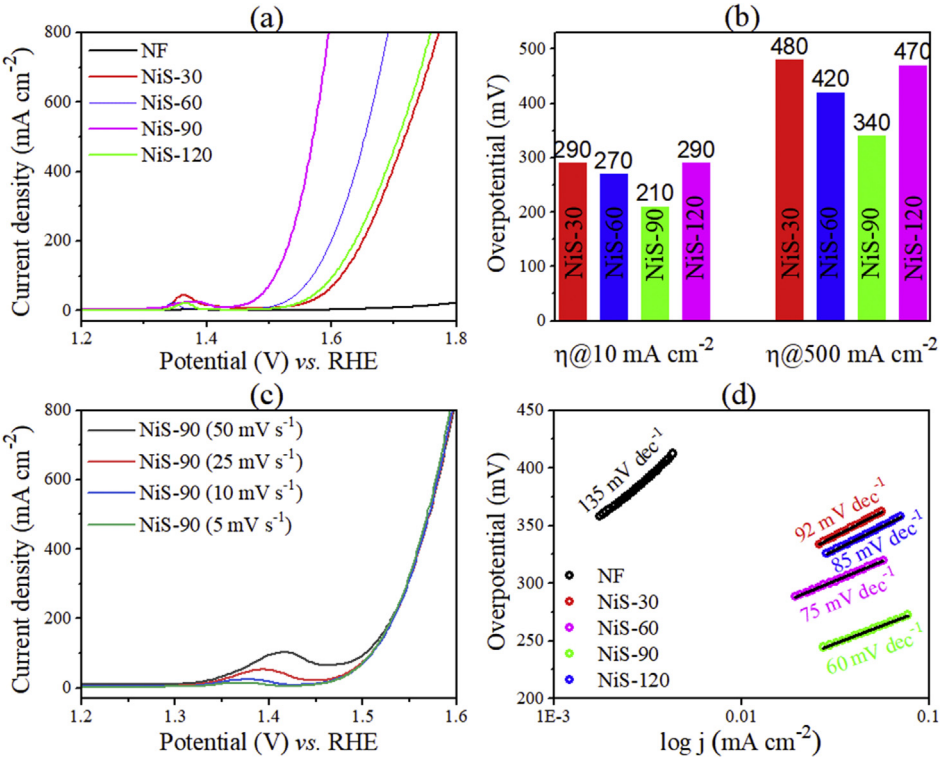

Fig. 6 – (a) Polarization curves for different NiS catalysts obtained at scan rate of 5 mV s^{-1}, (b) comparison of overpotential values of NiS catalyst to reach benchmark current densities of 10 and 500 mA cm^{-2}, (c) polarization curves of best OER activity of NiS-90 catalyst recorded at different scan rates of 50, 25 10 and 5 mV s^{-1} and (d) Tafel plot indicating the OER kinetics for all NiS catalyst.

The enhanced OER activity of the electrochemically oxidized NiS-90 catalyst can be attributed to the unique and uniform fur-rug shaped microstructure shown in Fig. 2 (c). The catalytic centers appear to be more aligned and unidirectional, which provides a large contact area between the catalyst and reactant species. However, other NiS catalyst surfaces are less uniform as shown by the microstructure images in Fig. 2 ((a), (b) and (d)). Another factor that contributes to the improved OER performance of the NiS-90 catalyst could be the optimum mass loading of the catalyst (0.3 mg), which leads to its superior activity. Fig. 6 (c) shows the polarization curves recorded at different scan rates for the best performing NiS-90 catalyst and no apparent change in current density was identified at different scan rates. Tafel plots for all catalysts were made to study the OER kinetics. Fig. 6 (d) shows the Tafel plots obtained by fitting the linear parts of the polarization curves. Tafel slope values for bare NF, NiS-30, NiS-60, NiS-90 and NiS-120 were measured to be 92, 85, 75 and 60 mV dec^{-1}, respectively. The NiS-90 electrode had the lowest Tafel slope value (60 mV dec^{-1}), suggesting faster OER reaction kinetics, probably due to its uniform microstructure and optimal catalyst mass loading. In addition, the Tafel value of NiS-30 is close to that of NiS-120, suggesting similar pathways and rate determining steps for these electrodes in a similar alkaline environment.

It is common that the solution resistance is normally participated during measurement of OER activity of electrocatalysts and the electrocatalyst with low charge transfer resistance show high electrocatalytic activity for OER. EIS is used to measure the charge transfer resistance of electrocatalysts. So, the values of charge transfer resistance are measured by employing EIS and the EIS data are recorded as Nyquist plots using 1 M KOH as electrolyte solution at open circuit potential. The obtained results are presented in Fig. 7, which clearly indicates that the electrocatalyst NiS-90 has lower charge transfer resistance compared to other electrocatalysts, which further confirms its enhanced electrocatalytic activity for OER [66].

The OER parameters of the NiS-90 catalyst are compared to the reported data for various nickel sulfide phases fabricated from different processes, as shown in Table 1. The activity of the NiS catalyst prepared by AACVD is better than that mentioned in Table 1.

The electrocatalytic stability of the NiS-90 electrode with the best performance was also examined by galvanostatic chronopotentiometric measurements at two different applied current densities of 10 and 20 mA cm^{-2}, respectively. The resulting chronopotentiometric profile shown in Fig. 8 (a), revealed that the electrochemically oxidized Ni-sulfide catalyst was largely stable during the 19 h of the chronopotentiometric experiment. The η_{10} value at 10 mA cm^{-2} improved from 228 mV to 205 mV by the first 10 h. When switching the current density from 10 to 20 mA cm^{-2}, a small increase in the η_{10} value from 205 to 221 mV was found. The η_{20} value at 20 mA cm^{-2} hardly fluctuated and remained constant between 221 mV and 216 mV in last 9 h. The result shows that the overvoltage values remain

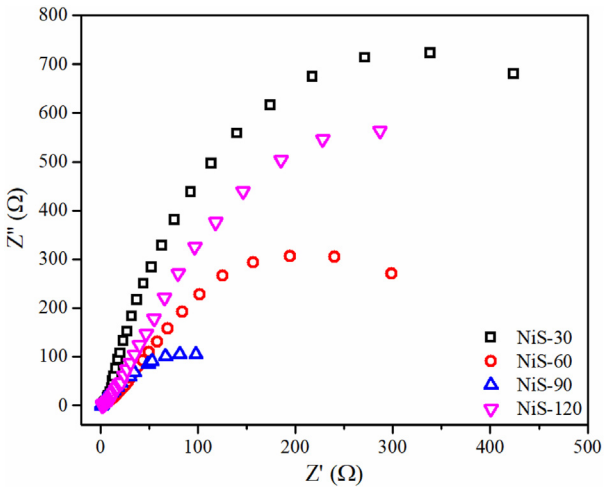

Fig. 7 – EIS Nyquist plots recorded in 1.0 M of KOH solution for NiS-30, NiS-60, NiS-90, and NiS-120 electrocatalysts loaded on NF.

almost constant with two different applied current densities and no signs of deterioration or delamination of the film electrode were found during the long-term stability test. After a chronopotentiometric experiment, the polarization curve of the same electrode was recoded and compared with its initial behavior. As shown in Fig. 8 (b), the current density of the NiS electrode is slightly increased after the stability. The small increment in current density is attributed to the reconstruction of the catalyst structure during the long-term stability test. This behavior agrees with the reported nickel sulfide catalyst [41].

The turnover frequency (TOF, per catalyst site) was estimated using the equation [TOF = I/(4 × F × m)]. Where I, F and m are the current, Faraday's constant (96,485 C/mol) and number of moles of active material (catalyst) that is deposited on the electrode respectively. The TOF at overpotentials of 210 mV and 340 mV was calculated for the NiS-90 electrocatalyst and its values were found to be 0.01 s^{-1} and 0.39 s^{-1} respectively, which is comparable to some reported electrocatalysts [71,72].

The surface of the used NiS-90 catalyst was re-examined by FESEM and EDX analyses to observe any morphological and compositional changes induced by the prolonged electrochemical treatment. Fig. 9 shows the FESEM images of the used catalyst surface. It can be clearly observed that the catalyst retained its spike and thorn-like microstructure as observed in its fresh form (Fig. 2 (c)). In some spots the spiky structure is not visible due to the build-up of the electrolyte (KOH) mass. The elemental composition of the Ni, S, O and K atoms on the surface of the used NiS-90 catalyst was also determined. Fig. 10

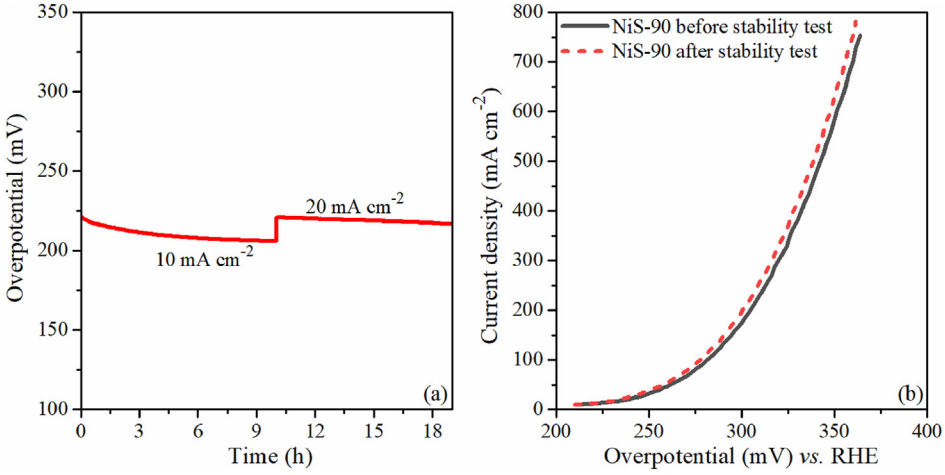

Fig. 8 – (a) Extended period of oxygen evolution during controlled potential electrolysis of NiS-90 catalyst in 1.0 M KOH electrolyte solution at two different current densities, (b) LSV polarization curves of NiS-90 catalyst before and after stability test.

Table 1 – Comparison of OER parameters of NiS catalysts produced from different fabrication methods.

Catalyst material	Synthesis route	Overpotential (mV) @ 10 mA cm^{-2}	Reference
Ni_2S_3	Thermal sulfurization	256	[65]
NiS	Sulfurization	335	[43]
Ni_3S_2	Hydrothermal	344	[45]
NiS		375	[38]
Ni_3S_2	Polyol solution method	295	
NiS_2		375	
Ni_3S_2/NiFe layer double hydroxide	Electrodeposited	200	[67]
Ni/NiS//N-doped carbon	High temperature treatment	337	[68]
IrO_2	Commercially available	301	[69]
RuO_2	Commercially available	322	[70]
NiS-90	AACVD	210	This work

(a1 and a2) shows the EDX spectrum that was recorded from two different points with their respective elemental compositions. The used NiS-90 catalyst has significantly reduced the S content as compared to its unused form (EDX spectrum Fig. 3 (c)). While the O contents, which was completely absent on the surface of fresh catalyst, increased significantly in used

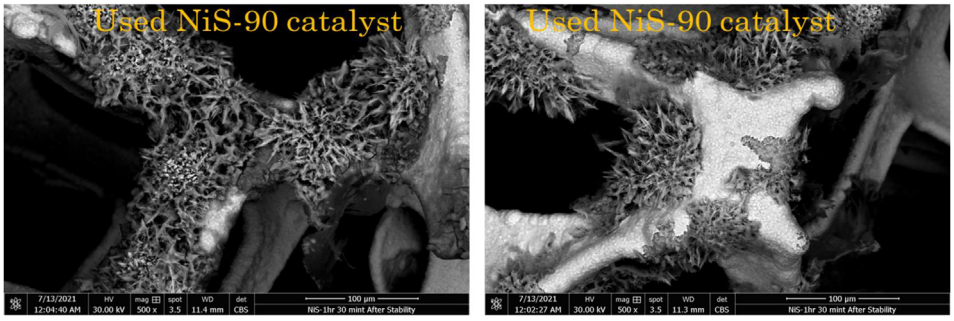

Fig. 9 – Low-magnification FESEM images of used NiS-90 catalyst taken at different places.

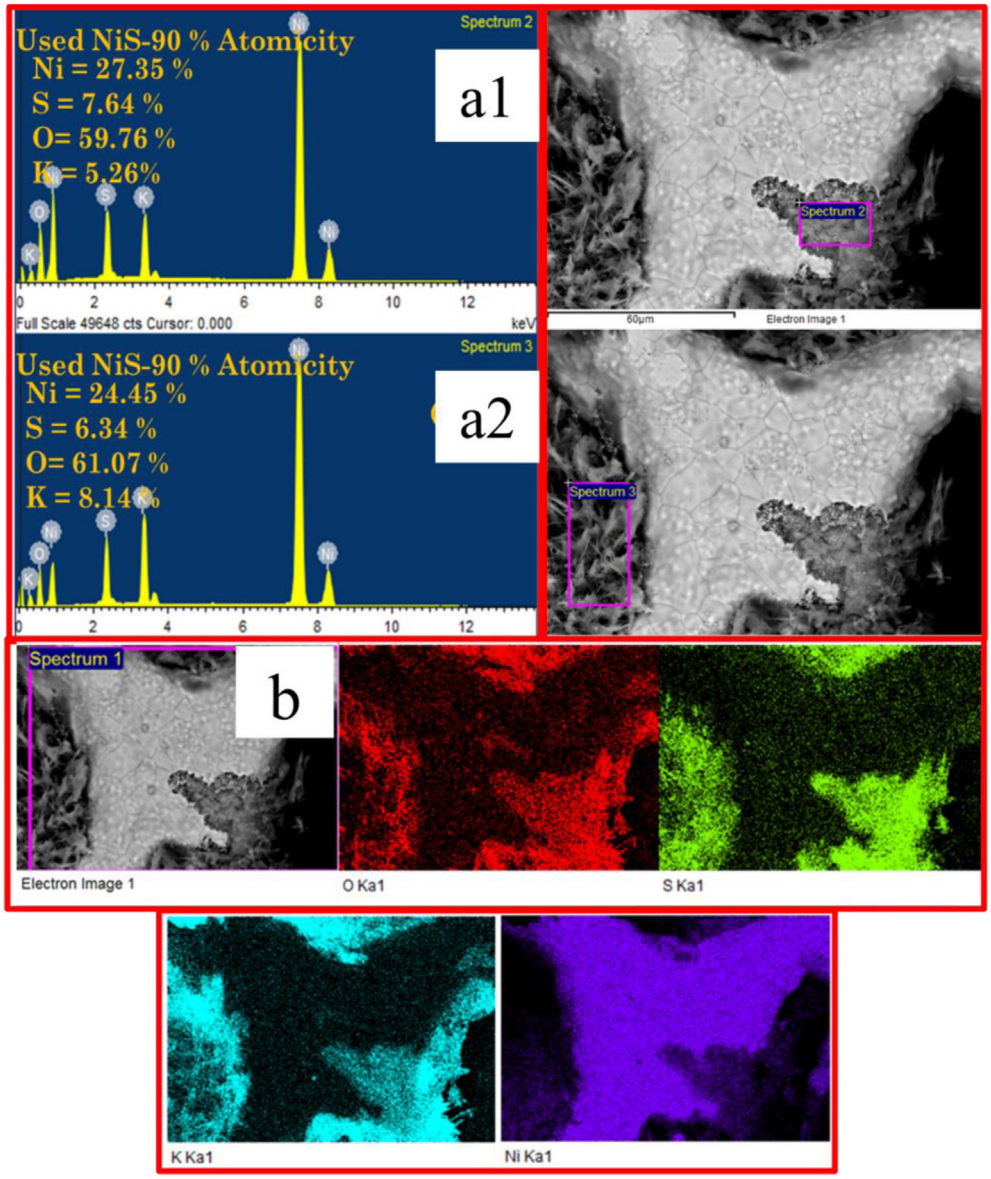

Fig. 10 – EDX spectra of used NiS-90 catalyst analyzed at two different surfaces (a1 and a2) and EDX map analysis indicating the homogenous distribution of Ni, O, S and K atoms on the surface of used NiS-90 catalyst (b).

catalyst. In addition, an EDX map analysis was performed to identify the positions of the S and O atoms, and a homogenous distribution of both elements can be analyzed using the EDX map images given in Fig. 10 (b). The presence of S together with O atoms evidences that NiS catalyst was partially oxidized during the electrochemical OER process, as opposed to the complete removal of the sulfide ions from the catalyst surface, which resulted in a complete conversion of NiS to amorphous NiO, such as described in an earlier study [49,65].

Finally, an XRD analysis of used NiS-90 was performed and the result is shown in Fig. 11. The XRD pattern indicates the formation of several nickel oxide phases including "NiO_2", "$K_3Ni_2O_4$" and "$K_{0.14}NiO_2$" due to electrochemical treatment. Some crystalline peaks related to metallic "Ni" are appeared from nickel foam substrate. No peaks related to the initial "NiS" phase were identified. Based on post-characterization results (XRD and EDX), a hypothetical mechanism for water oxidation on the surface of NiS electrocatalyst was proposed. During water oxidation process, the sulfide species are leached out from the film surface and the electrode surface is transformed into highly reactive "oxo" and "oxyhydroxide" intermediate spices as indicated by the following pathways which include unusual and mixed valence states of nickel ions such as Ni°, Ni^{+}, Ni^{2+} and Ni^{4+}:

$$4OH^- \rightarrow O_2 + 2H_2O + 4\,e^-$$

$$VOH^- \rightarrow OH^* + e^-;\ OH^* \rightarrow O^* + H+ + e^-$$

$$2O^* \rightarrow O_2 \text{ or } O^* + OH^- \rightarrow {}^*OOH + e^-$$

$$^*OOH + OH^- \rightarrow O_2 + H_2O + e^-$$

The larger the surface oxide layers on Ni–S, the OER and its stability will be greatly facilitated. Moreover, the synergetic chemical coupling effects of different nickel oxide phases also make a positive contribution to the OER performance. This proposed mechanism is also supported by the earlier study based on nickel sulfide over NF surface to improve OER activity [65,73,74].

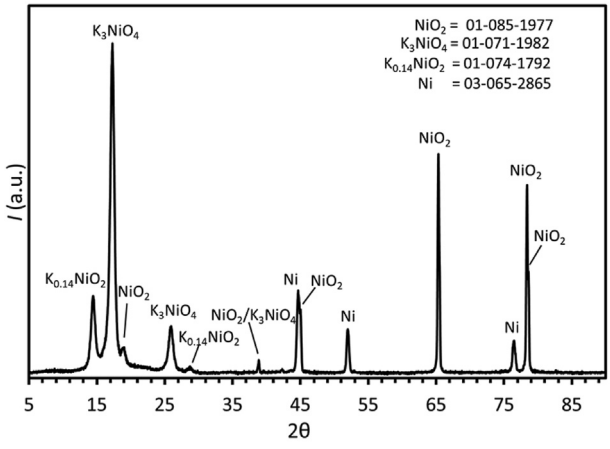

Fig. 11 – XRD pattern of the used NiS-90 catalyst after performing electrochemical water oxidation in 1 M KOH electrolyte.

Conclusions

In summary, the deposition of NiS nanowires on the surface of nickel foam using a simple, fast and one-step method of aerosol-assisted chemical vapor deposition has been successfully demonstrated. The various NiS catalysts, developed for 30, 60, 90 and 120 min, showed great potential for OER water electrolysis in an alkaline medium. The NiS catalyst obtained in 90 min of deposition exhibited relatively small overpotential values of 210 and 340 mV in order to approximate the characteristic current densities of 10 and 500 mA cm^{-2}, respectively. In addition, the catalyst was durable and sustainable enough to continuously catalyze the OER for 19 h. The high OER performance of the NiS catalyst is related to the partial conversion of nickel sulfide to nickel oxide during the electrochemical activation process. The electrochemical and structural characterization suggested that S atoms near the surface of NiS acted as an activator to generate important oxidized $Ni(OH)_2$/NiOOH intermediates that promote water oxidation by providing numerous active sites and thus result in a significant improvement in OER performance. This study provides important insight into the nickel sulfide electrocatalyst for water oxidation. Moreover, the NiS nanowires are considered promising electrode materials for several other applications such as batteries, supercapacitor, and fuel cells, etc.

Declaration of competing interest

The authors declare that they have no known competing financial interests or personal relationships that could have appeared to influence the work reported in this paper.

Acknowledgments

The authors greatly acknowledge the characterization facilities provided at the Interdisciplinary Research Center-Hydrogen and Energy Storage (IRC-HES), of King Fahd University of Petroleum and Minerals (KFUPM).

REFERENCES

[1] Abe JO, Popoola API, Ajenifuja E, Popoola OM. Hydrogen energy, economy and storage: review and recommendation. Int J Hydrogen Energy 2019;44:15072–86.
[2] Nazir H, Louis C, Jose S, Prakash J, Muthuswamy N, Buan MEM, et al. Is the H_2 economy realizable in the foreseeable future? Part I: H_2 production methods. Int J Hydrogen Energy 2020;45:13777–88.
[3] Dawood F, Anda M, Shafiullah GM. Hydrogen production for energy: an overview. Int J Hydrogen Energy 2020;45:3847–69.
[4] Aziz M, Wijayanta AT, Nandiyanto ABD. Ammonia as effective hydrogen storage: a review on production, storage and utilization. Energies 2020;13:3062.
[5] Sazali N. Emerging technologies by hydrogen: a review. Int J Hydrogen Energy 2020;45:18753–71.

[6] Li Y, Li R, Wang D, Xu H, Meng F, Dong D, Jiang J, Zhang J, An M, Yang P. A review: target-oriented transition metal phosphide design and synthesis for water splitting. Int J Hydrogen Energy 2021;46:5131–49.
[7] Chen G, Hu Z, Zhu Y, Gu B, Zhong Y, Lin HJ, Chen CT, Zhou W, Shao Z. A universal strategy to design superior water-splitting electrocatalysts based on fast in situ reconstruction of amorphous nanofilm precursors. Adv Mater 2018;30:1804333.
[8] Anantharaj S, Ede SR, Sakthikumar K, Karthick K, Mishra S, Kundu S. Recent trends and perspectives in electrochemical water splitting with an emphasis on sulfide, selenide, and phosphide catalysts of Fe, Co, and Ni: a review. ACS Catal 2016;6:8069–97.
[9] Shi Q, Zhu C, Du D, Lin Y. Robust noble metal-based electrocatalysts for oxygen evolution reaction. Chem Soc Rev 2019;48:3181–92.
[10] Shang X, Tang J-H, Dong B, Sun Y. Recent advances of nonprecious and bifunctional electrocatalysts for overall water splitting. Sustain Energy Fuels 2020;4:3211–28.
[11] Li J, Zheng G. One-dimensional earth-abundant nanomaterials for water-splitting electrocatalysts. Adv Sci 2017;4:1600380.
[12] Shang X, Dong B, Chai Y-M, Liu C-G. In-situ electrochemical activation designed hybrid electrocatalysts for water electrolysis. Sci Bull 2018;63:853–76.
[13] Liang H, Xu M, Asselin E. Corrosion of monometallic iron- and nickel-based electrocatalysts for the alkaline oxygen evolution reaction: a review. J Power Sources 2021;510:230387.
[14] Ye W, Fang X, Chen X, Yan D. A three-dimensional nickel–chromium layered double hydroxide micro/nanosheet array as an efficient and stable bifunctional electrocatalyst for overall water splitting. Nanoscale 2018;10:19484–91.
[15] Shen J, Zhang P, Xie R, Chen L, Li M, Li J, Ji B, Hu Z, Li J, Song L, Wu Y, Zhao X. Controlled self-assembled NiFe layered double hydroxides/reduced graphene oxide nanohybrids based on the solid-phase exfoliation strategy as an excellent electrocatalyst for the oxygen evolution reaction. ACS Appl Mater Interfaces 2019;11:13545–56.
[16] Jin X, Shin S-J, Kim J, Lee N-S, Kim H, Hwang S-J. Heterolayered 2D nanohybrids of uniformly stacked transition metal dichalcogenide–transition metal oxide monolayers with improved energy-related functionalities. J Mater Chem 2018;6:15237–44.
[17] Zhou W, Zhao M, Liang F, Smith SC, Zhu Z. High activity and durability of novel perovskite electrocatalysts for water oxidation. Mater Horiz 2015;2:495–501.
[18] Xu X, Wang W, Zhou W, Shao Z. Recent advances in novel nanostructuring methods of perovskite electrocatalysts for energy-related applications. Small Methods 2018;2:1800071.
[19] Wu X, Yu J, Yang G, Liu H, Zhou W, Shao Z. Perovskite oxide/carbon nanotube hybrid bifunctional electrocatalysts for overall water splitting. Electrochim Acta 2018;286:47–54.
[20] Peng X, Yan Y, Jin X, Huang C, Jin W, Gao B, Chu PK. Recent advance and prospectives of electrocatalysts based on transition metal selenides for efficient water splitting. Nanomater Energy 2020;78:105234.
[21] Wang B, Hu Y, Yu B, Zhang X, Yang D, Chen Y. Heterogeneous CoFe–Co_8FeS_8 nanoparticles embedded in CNT networks as highly efficient and stable electrocatalysts for oxygen evolution reaction. J Power Sources 2019;433:126688.
[22] Al-Enizi AM, Shaikh SF, Ubaidullah M, Ghanem MA, Mane RS. Self-grown one-dimensional nickel sulfo-selenide nanostructured electrocatalysts for water splitting reactions. Int J Hydrogen Energy 2020;45:15904–14.
[23] Jia X, Wang M, Liu G, Wang Y, Yang J, Li J. Mixed-metal MOF-derived Co-doped Ni_3C/Ni NPs embedded in carbon matrix as an efficient electrocatalyst for oxygen evolution reaction. Int J Hydrogen Energy 2019;44:24572–9.
[24] Farid S, Ren S, Tian D, Qiu W, Zhao J, Zhao L, Mao Q, Hao C. 3D flower-like polypyrrole-derived N-doped porous carbon coupled cobalt oxide as efficient oxygen evolution electrocatalyst. Int J Hydrogen Energy 2020;45:31926–41.
[25] Qian H, Li K, Mu X, Zou J, Xie S, Xiong X, Zeng X. Nanoporous NiFeMoP alloy as a bifunctional catalyst for overall water splitting. Int J Hydrogen Energy 2020;45:16447–57.
[26] Wang Y, Kong B, Zhao D, Wang H, Selomulya C. Strategies for developing transition metal phosphides as heterogeneous electrocatalysts for water splitting. Nano Today 2017;15:26–55.
[27] Guo R, Lai X, Huang J, Du X, Yan Y, Sun Y, Zou G, Xiong J. Phosphate-based electrocatalysts for water splitting: recent progress. ChemElectroChem 2018;5:3822–34.
[28] Peng W, Zheng G, Wang Y, Cao S, Ji Z, Huan Y, Zou M, Yan X. Zn doped ZIF67-derived porous carbon framework as efficient bifunctional electrocatalyst for water splitting. Int J Hydrogen Energy 2019;44:19782–91.
[29] Ye W, Yang Y, Fang X, Arif M, Chen X, Yan D. 2D Cocrystallized metal–organic nanosheet array as an efficient and stable bifunctional electrocatalyst for overall water splitting. ACS Sustainable Chem Eng 2019;7:18085–92.
[30] Yan Y, He T, Zhao B, Qi K, Liu H, Xia BY. Metal/covalent–organic frameworks-based electrocatalysts for water splitting. J Mater Chem A 2018;6:15905–26.
[31] Zhou Y-N, Yu W-L, Cao Y-N, Zhao J, Dong B, Ma Y, Wang F-L, Fan R-Y, Zhou Y-L, Chai Y-M. S-doped nickel-iron hydroxides synthesized by room-temperature electrochemical activation for efficient oxygen evolution. Appl Catal B Environ 2021;292:120150.
[32] Yan K-L, Qin J-F, Liu Z-Z, Dong B, Chi J-Q, Gao W-K, Lin J-H, Chai Y-M, Liu C-G. Organic-inorganic hybrids-directed ternary NiFeMoS anemone-like nanorods with scaly surface supported on nickel foam for efficient overall water splitting. Chem Eng J 2018;334:922–31.
[33] Shang X, Yan K-L, Rao Y, Dong B, Chi J-Q, Liu Y-R, et al. In situ cathodic activation of V-incorporated Ni_xS_y nanowires for enhanced hydrogen evolution. Nanoscale 2017;9:12353–63.
[34] Vij V, Sultan S, Harzandi AM, Meena A, Tiwari JN, Lee W-G, Yoon T, Kim KS. Nickel-based electrocatalysts for energy-related applications: oxygen reduction, oxygen evolution, and hydrogen evolution reactions. ACS Catal 2017;7:7196–225.
[35] Yu XY, Lou XW. Mixed metal sulfides for electrochemical energy storage and conversion. Adv Energy Mater 2018;8:1701592.
[36] Sun H, Yan Z, Liu F, Xu W, Cheng F, Chen J. Self-supported transition-metal-based electrocatalysts for hydrogen and oxygen evolution. Adv Mater 2020;32:1806326.
[37] Dong B, Zhao X, Han G-Q, Li X, Shang X, Liu Y-R, Hu W-H, Chai Y-M, Zhao H, Liu C-G. Two-step synthesis of binary Ni–Fe sulfides supported on nickel foam as highly efficient electrocatalysts for the oxygen evolution reaction. J Mater Chem A 2016;4:13499–508.
[38] Zheng X, Han X, Zhang Y, Wang J, Zhong C, Deng Y, Hu W. Controllable synthesis of nickel sulfide nanocatalysts and their phase-dependent performance for overall water splitting. Nanoscale 2019;11:5646–54.
[39] Jiang N, Tang Q, Sheng M, You B, Jiang D-e, Sun Y. Nickel sulfides for electrocatalytic hydrogen evolution under alkaline conditions: a case study of crystalline NiS, NiS_2, and Ni_3S_2 nanoparticles. Catal Sci Technol 2016;6:1077–84.
[40] Yao M, Sun B, He L, Wang N, Hu W, Komarneni S. Self-assembled Ni_3S_2 nanosheets with mesoporous structure

tightly held on Ni foam as a highly efficient and long-term electrocatalyst for water oxidation. ACS Sustainable Chem Eng 2019;7:5430–9.
[41] Chaudhari NK, Jin H, Kim B, Lee K. Nanostructured materials on 3D nickel foam as electrocatalysts for water splitting. Nanoscale 2017;9:12231–47.
[42] Wu F, Guo X, Hao G, Hu Y, Jiang W. Synthesis of iron–nickel sulfide porous nanosheets via a chemical etching/anion exchange method for efficient oxygen evolution reaction in alkaline media. Adv Mater Interfaces 2019;6:1900788.
[43] Zhu W, Yue X, Zhang W, Yu S, Zhang Y, Wang J, Wang J. Nickel sulfide microsphere film on Ni foam as an efficient bifunctional electrocatalyst for overall water splitting. Chem Commun 2016;52:1486–9.
[44] Liu M, Jiao Y, Zhan S, Wang H. Ni_3S_2 nanowires supported on Ni foam as efficient bifunctional electrocatalyst for urea-assisted electrolytic hydrogen production. Catal Today 2020;355:596–601.
[45] Wang X, Wang S, Chen S, He P, Xu Y, Jia L, Yang D, He X, Deng H, Jia B. Facile one-pot synthesis of binder-free nano/micro structured dendritic cobalt activated nickel sulfide: a highly efficient electrocatalyst for oxygen evolution reaction. Int J Hydrogen Energy 2020;45:19304–12.
[46] Gong Y, Lin Y, Yang Z, Jiao F, Li J, Wang W. High-performance bifunctional flower-like Mn-doped $Cu_{7.2}S_4$@NiS_2@NiS/NF catalyst for overall water splitting. Appl Surf Sci 2019;476:840–9.
[47] Zhou W, Wu X-J, Cao X, Huang X, Tan C, Tian J, et al. Ni_3S_2 nanorods/Ni foam composite electrode with low overpotential for electrocatalytic oxygen evolution. Energy Environ Sci 2013;6:2921–4.
[48] Li C, Zhao X, Liu Y, Wei W, Lin Y. 3D Ni-Co sulfoxide nanosheet arrays electrodeposited on Ni foam: a bifunctional electrocatalyst towards efficient and stable water splitting. Electrochim Acta 2018;292:347–56.
[49] Mabayoje O, Shoola A, Wygant BR, Mullins CB. The role of anions in metal chalcogenide oxygen evolution catalysis: electrodeposited thin films of nickel sulfide as "pre-catalysts". ACS Energy Lett 2016;1:195–201.
[50] Zahran ZN, Mohamed EA, Tsubonouchi Y, Ishizaki M, Togashi T, Kurihara M, et al. Electrocatalytic water splitting with unprecedentedly low overpotentials by nickel sulfide nanowires stuffed into carbon nitride scabbards. Energy Environ Sci 2021;14:5358–65.
[51] Gervas C, Mlowe S, Akerman MP, Revaprasadu N. Phase pure Ni 3 S 2 and NiS from bis (N′-ethyl-N-piperazinylcarbodithioato-S, S′)–nickel (ii) via solvent thermolysis and aerosol assisted chemical vapour deposition. New J Chem 2018;42:6203–9.
[52] Alam N, Hill MS, Kociok-Köhn G, Zeller M, Mazhar M, Molloy KC. Pyridine adducts of nickel (II) xanthates as single-source precursors for the aerosol-assisted chemical vapor deposition of nickel sulfide. Chem Mater 2008;20:6157–62.
[53] Mgabi L, Dladla B, Malik M, Garje SS, Akhtar J, Revaprasadu N. Deposition of cobalt and nickel sulfide thin films from thio-and alkylthio-urea complexes as precursors via the aerosol assisted chemical vapour deposition technique. Thin Solid Films 2014;564:51–7.
[54] Ehsan MA, Adam A, Rehman A, Hakeem AS, Isab AA, Qamar M. Morphologically controlled rapid fabrication of rhodium sulfide (Rh_2S_3) thin films for superior and robust hydrogen evolution reaction. Sustain Energy Fuels 2021;5:459–68.
[55] Ehsan M, Adam A, Rehman A, Qamar M. Direct self-assembly of hierarchically grown rhodium thin films for electrocatalytic hydrogen evolution reaction. Catalysts 2021;11:338.
[56] Joya KS, Ehsan MA, Sohail M, Yamani ZH. Nanoscale palladium as a new benchmark electrocatalyst for water oxidation at low overpotential. J Mater Chem 2019;7:9137–44.
[57] Ehsan MA, Hakeem AS, Rehman A. Synergistic effects in bimetallic Pd–CoO electrocatalytic thin films for oxygen evolution reaction. Sci Rep 2020;10:1–11.
[58] Wang P, Zhang X, Zhang J, Wan S, Guo S, Lu G, Yao J, Huang X. Precise tuning in platinum-nickel/nickel sulfide interface nanowires for synergistic hydrogen evolution catalysis. Nat Commun 2017;8:14580.
[59] Zhao S, Ying Z, Yang J, Fan C, Zhang W. Novel nickel foam@carbon microspheres@Ni_3S_2 composite electrode for high-performance supercapacitors. Mater Lett 2016;183:437–40.
[60] Xu R, Zhou Q, Li F, Zhang B. Laccase immobilization on chitosan/poly(vinyl alcohol) composite nanofibrous membranes for 2,4-dichlorophenol removal. Chem Eng J 2013;222:321–9.
[61] Hu P, Wang T, Zhao J, Zhang C, Ma J, Du H, et al. Ultrafast alkaline Ni/Zn battery based on Ni-foam-supported Ni_3S_2 nanosheets. ACS Appl Mater Interfaces 2015;7:26396–9.
[62] Li T, Zuo Y, Lei X, Li N, Liu J, Han H. Regulating the oxidation degree of nickel foam: a smart strategy to controllably synthesize active Ni_3S_2 nanorod/nanowire arrays for high-performance supercapacitors. J Mater Chem 2016;4:8029–40.
[63] Trotochaud L, Young SL, Ranney JK, Boettcher SW. Nickel–iron oxyhydroxide oxygen-evolution electrocatalysts: the role of intentional and incidental iron incorporation. J Am Chem Soc 2014;136:6744–53.
[64] Louie MW, Bell AT. An investigation of thin-film Ni–Fe oxide catalysts for the electrochemical evolution of oxygen. J Am Chem Soc 2013;135:12329–37.
[65] Lee M, Oh H-S, Cho MK, Ahn J-P, Hwang YJ, Min BK. Activation of a Ni electrocatalyst through spontaneous transformation of nickel sulfide to nickel hydroxide in an oxygen evolution reaction. Appl Catal B Environ 2018;233:130–5.
[66] Khan NA, Rashid N, Junaid M, Zafar MN, Faheem M, Ahmad I. NiO/NiS Heterostructures: an efficient and stable electrocatalyst for oxygen evolution reaction. ACS Appl Energy Mater 2019;2:3587–94.
[67] Liang Z, Zhou P, Wang Z, Wang P, Liu Y, Qin X, Zhang X, Dai Y, Zheng Z, Huang B. Electrodeposition of NiFe layered double hydroxide on Ni3S2 nanosheets for efficient electrocatalytic water oxidation. Int J Hydrogen Energy 2020;45:8659–66.
[68] Ding J, Ji S, Wang H, Gai H, Liu F, Linkov V, Wang R. Mesoporous nickel-sulfide/nickel/N-doped carbon as HER and OER bifunctional electrocatalyst for water electrolysis. Int J Hydrogen Energy 2019;44:2832–40.
[69] Luo F, Zhang Q, Yu X, Xiao S, Ling Y, Hu H, Guo L, Yang Z, Huang L, Cai W, Cheng H. Palladium phosphide as a stable and efficient electrocatalyst for overall water splitting. Angew Chem Int Ed 2018;57:14862–7.
[70] Hyun S, Shanmugam S. Hierarchical nickel–cobalt dichalcogenide nanostructure as an efficient electrocatalyst for oxygen evolution reaction and a Zn–air battery. ACS Omega 2018;3:8621–30.
[71] Wang S, Lu A, Zhong C-J. Hydrogen production from water electrolysis: role of catalysts. Nano Convergence 2021;8:4.
[72] Sahoo PK, Bisoi SR, Huang Y-J, Tsai D-S, Lee C-P. 2D-Layered non-precious electrocatalysts for hydrogen evolution reaction: fundamentals to applications. Catalysts 2021;11:689.
[73] Zhou W, Cao X, Zeng Z, Shi W, Zhu Y, Yan Q, et al. One-step synthesis of Ni_3S_2 nanorod@$Ni(OH)_2$ nanosheet core–shell nanostructures on a three-dimensional graphene network for high-performance supercapacitors. Energy Environ Sci 2013;6:2216–21.
[74] Yin J, Li Y, Lv F, Lu M, Sun K, Wang W, Wang L, Cheng F, Li Y, Xi P, Guo S. Oxygen vacancies dominated NiS_2/CoS_2 interface porous nanowires for portable Zn-air batteries driven water splitting devices. Adv Mater 2017;29:04681.